

GAMBAS: Generalised-Hilbert Mamba for Super-resolution of Paediatric Ultra-Low-Field MRI

Levente Baljer^{*1,2}

Ula Briski¹

Robert Leech¹

Niall J Bourke¹

Kirsten A Donald³

Layla E Bradford³

Simone R Williams³

Sadia Parkar⁴

Sidra Kaleem⁴

Salman Osmani⁴

Sean CL Deoni⁵

Steven CR Williams¹

Rosalyn J Moran^{†1}

Emma C Robinson^{†2}

František Váša^{†1}

LEVENTE.1.BALJER@KCL.AC.UK

ULA.BRISKI@KCL.AC.UK

ROBERT.LEECH@KCL.AC.UK

NIALL.BOURKE@KCL.AC.UK

KIRSTEN.DONALD@UCT.AC.ZA

LAYLA.BRADFORD@UCT.AC.ZA

SIMONE.WILLIAMS@UCT.AC.ZA

SADIA.PARKAR@AKU.EDU

SIDRA.KALEEM@AKU.EDU

SALMAN.OSMANI@AKU.EDU

SEAN.DEONI@GATESFOUNDATION.ORG

STEVE.WILLIAMS@KCL.AC.UK

ROSALYN.MORAN@KCL.AC.UK

EMMA.ROBINSON@KCL.AC.UK

FRANTISEK.VASA@KCL.AC.UK

¹ Department of Neuroimaging, King’s College London

² Department of Biomedical Computing, King’s College London

³ Department of Paediatrics and Child Health, University of Cape Town

⁴ Paediatrics and Child Health, Aga Khan University Hospital, Karachi

⁵ Bill & Melinda Gates Foundation, Seattle, Washington, USA

Editors: Accepted for publication at MIDL 2025

Abstract

Magnetic resonance imaging (MRI) is critical for neurodevelopmental research, however access to high-field (HF) systems in low- and middle-income countries is severely hindered by their cost. Ultra-low-field (ULF) systems mitigate such issues of access inequality, however their diminished signal-to-noise ratio limits their applicability for research and clinical use. Deep-learning approaches can enhance the quality of scans acquired at lower field strengths at no additional cost. For example, Convolutional neural networks (CNNs) fused with transformer modules have demonstrated a remarkable ability to capture both local information and long-range context. Unfortunately, the quadratic complexity of transformers leads to an undesirable trade-off between long-range sensitivity and local precision. We propose a hybrid CNN and state-space model (SSM) architecture featuring a novel 3D to 1D serialisation (GAMBAS), which learns long-range context without sacrificing spatial precision. We exhibit improved performance compared to other state-of-the-art medical image-to-image translation models. Our code is made publicly available at <https://github.com/levente-1/GAMBAS>.

Keywords: Mamba, Hilbert curve, MRI, Deep Learning, Image Quality Transfer.

* Corresponding author

† Joint senior authors

1. Introduction

High-field (HF) MRI (>1 T) is vital for radiation-free neurodevelopmental research and clinical assessment. Unfortunately, the high cost of scanners ($\sim \$1,000,000$ per Tesla; [Arnold et al. 2023](#)) and corresponding infrastructural requirements result in significant access inequalities across the globe. When comparing access to imaging via MRI units per million population, over a hundred-fold difference is exhibited between high-income countries (HICs) and low- and middle-income countries (LMICs) (e.g. 51.67 units/million in the US vs 0.48 units/million in Ghana; [Jalloul et al. 2023](#)).

Ultra-low-field (ULF) imaging systems (<0.1 T) present a potential solution to issues of access inequality. By relying on large, permanent magnets, they are significantly cheaper and easier to purchase and run than HF systems ([Campbell-Washburn et al., 2019](#)). Additionally, their reduced acoustic noise and open design increase patient compliance, especially in paediatric populations in whom the risk of head motion is naturally higher ([Padormo et al., 2023](#)). Unfortunately, these benefits come at the cost of reduced signal-to-noise ratio (SNR) and resolution, which renders images suboptimal for visual reading by radiologists or for many currently available processing methods.

Super-resolution (SR) techniques may help bridge the gap between ULF and HF, with deep learning being particularly well-suited to handle the nonlinear differences in tissue contrast between field strengths. Convolutional neural networks (CNNs) have historically dominated the field of medical image translation ([Wang et al., 2022](#)), with adversarial training schemes using an added discriminator further enhancing the perceptual quality of outputs ([Armanious et al., 2020](#)). CNNs exploit correlations among neighbouring voxels by extracting local features with compact filters. This reduces model complexity, however it limits the ability to model long-range spatial dependencies present in spatially-distributed brain structures, such as white matter or cerebrospinal fluid ([Wang and Wu, 2023](#)).

Vision transformers (ViTs) have shown an increased capacity to capture long-range context. By tokenizing an image into a sequence of patches and computing inter-patch similarity via attention operators, transformers learn to capture spatial correlations among distant regions ([Dosovitskiy et al., 2021](#)). Unfortunately, transformers exhibit quadratic model complexity with respect to sequence length (i.e. number of patches), impeding the use of patches small enough to maintain high spatial precision. State-space models (SSMs) offer a more efficient alternative for capturing long-range dependencies. They replace computationally expensive self-attention with linear recurrence, permitting images to be fed into the model as a sequence of individual voxels. Mamba, a variant of traditional SSMs with a powerful selection mechanism, has demonstrated impressive performance in a variety of medical imaging tasks, including segmentation, registration and classification ([Heidari et al., 2024](#)).

Here we introduce GAMBAS, **Generalised-Hilbert Mamba Super-resolution**, trained on paired paediatric ULF and HF scans (64mT and 3T, respectively). We fuse elements of CNNs with those of Mamba to increase model sensitivity to local and global context, and add adversarial learning to further increase output realism. We additionally present a novel serialisation approach that mitigates the loss of spatial proximity in Mamba layers. Our results indicate that GAMBAS offers superior performance against state-of-the-art (SOTA) transformer- and SSM-based models.

2. Related Work

Several works investigate translation between anisotropic 64mT and isotropic >1T brain MRI. SynthSR (Iglesias et al., 2021) employs a U-Net, trained using synthetic low-resolution scans generated from HF segmentations, to super-resolve images of any contrast and resolution, whereas LF-SynthSR (Iglesias et al., 2023) is a dedicated ULF version of the same network. LoHiResGAN (Islam et al., 2023) is an adversarial model with a ResNet-based generator (He et al., 2016), trained on 37 paired 64mT and 3T scans (T_{1w} and T_{2w}). SFNet (Tapp et al., 2024) is another adversarial model, using a SwinUNETR-V2 (He et al., 2023) generator trained on 30 empirical ULF/HF pairs combined with 60 synthetic pairs generated using a two-channel latent diffusion model.

3. Methods

3.1. Preliminaries

3.1.1. STATE-SPACE MODELS

The state space model (SSM) is a continuous-time latent state model, which maps a 1D input to a 1D output via a linear ordinary differential equation (ODE). Mamba is a specific SSM variant that discretises the ODE using the zero-order hold (ZOH) technique to produce an efficient recurrent formulation, and adds a selective scan algorithm to filter relevant/irrelevant information (see Appendix A for a derivation of Mamba from continuous-time SSMs). Importantly, Mamba demonstrates an ability to model long-range dependencies on par with that of Transformers, while reducing computational complexity (Gu and Dao, 2023).

As Mamba is designed to process 1D data, its application to vision tasks requires image features of shape (B, C, H, W, D) to be flattened and transposed to (B, L, C) , where $L = H \times W \times D$. Unlike input sequences in natural language processing tasks, images have no inherent directionality. As such, the approach used to arrange voxels into a 1D sequence determines the way Mamba processes the image and, in turn, affects overall model performance (Zhou et al., 2025).

3.1.2. SPACE-FILLING CURVES

Many approaches to flatten an image rely on a simple ‘Raster’ scan, which can result in discontinuities when the scan reaches the boundaries of the image. An alternative approach involves the use of space-filling curves, e.g. Z-order curve (Orenstein, 1986) or Hilbert curve (Hilbert 1891; see Figure 1 and Appendix B). Both curves provide a linear mapping between 3D and 1D space that preserves spatial locality (Moon et al., 2001), with the Hilbert curve demonstrating superior order-preserving behaviour (Warren and Salmon, 1993). Because of this property, it has been applied to point-cloud processing in conjunction with transformers (Chen et al., 2022) and, more recently, with Mamba (Zhang et al., 2024). Despite these successes, the fusion of the Hilbert curve with Mamba has not yet been demonstrated for medical image applications. Here, we apply a generalised variant of the Hilbert curve (“Gilbert”; Červený 2019), capable of handling evenly-sided 3D data of any size, to serialise structural MRI input into a 1D vector.

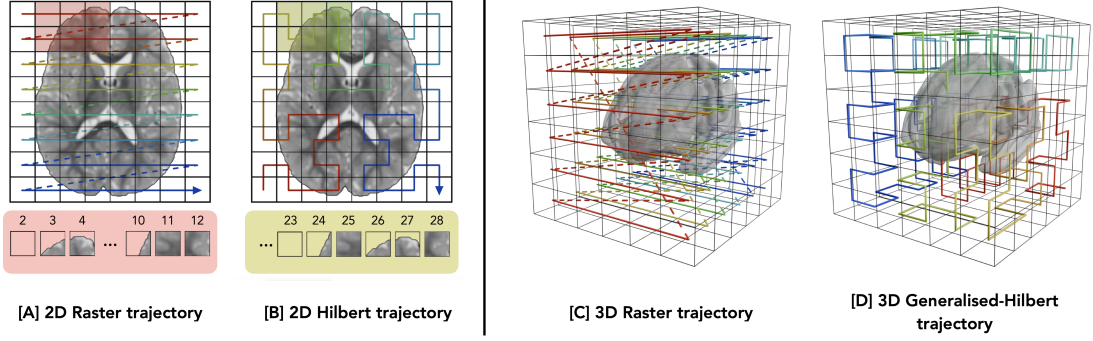


Figure 1: **Left:** [A] 2D Raster trajectory and [B] 2D Hilbert trajectory, with corresponding 2D \rightarrow 1D serialisation of highlighted region shown below. **Right:** [C] 3D Raster trajectory and [D] 3D Generalised-Hilbert trajectory.

3.2. Architecture

3.2.1. GAMBAS

We use a 3D counterpart of the 9-block ResNet architecture, originally introduced in [Zhu et al. 2017](#), as the backbone of GAMBAS. The model follows an encoder-decoder pathway (composed of 3 layers each) with an extended central bottleneck (consisting of 9 layers). The order of operations across layers is kept identical to the original paper, however all 2D convolutions are switched to their 3D counterparts, and batch normalisation is substituted with instance normalisation. Inspired by earlier work incorporating SSMs for 2D multi-modal medical image synthesis ([Atli et al., 2024](#)), we insert Mamba blocks into the 9-layer bottleneck, with the positioning determined via ablations studies (see Figure 2 and Appendix D). Through these blocks, encoder outputs are serialised via a generalised Hilbert trajectory, then fed into bidirectional Mamba modules. Outputs from Mamba are then concatenated with earlier CNN outputs and fed into channel-mixing blocks ([Dalmaz et al., 2022](#)) to consolidate contextual features from Mamba with structural features from CNNs. Channel-mixing blocks consist of two parallel convolutional branches of varying kernel sizes, mixing features at both identical and differing spatial locations ([Tolstikhin et al., 2021](#)).

3.2.2. TRAINING OBJECTIVE

We implement GAMBAS as an adversarial model, using PatchGAN as our discriminator ([Isola et al., 2017](#)). Once again, we keep operations identical to the original paper, switching only 2D convolutions to 3D convolutions and batch normalisation to instance normalisation. The discriminator has two input channels, taking in both an ULF scan and either a real or synthetic HF scan at each training step to determine whether the input pair is real. As such, our model follows the conditional GAN (cGAN) training objective, summarised by:

$$\mathcal{L}_{cGAN}(G, D) = \mathbb{E}_{x,y}[\log D(x, y)] + \mathbb{E}_x[\log 1 - D(x, (G(x)))] \quad (1)$$

where generator G and discriminator D aim to a minimise and maximise expectation \mathbb{E} , respectively. To ensure subject anatomy is maintained on conditional image generation, G is tasked with an additional loss of minimising the L1 distance between model outputs and reference HF images:

$$\mathcal{L}_{L1}(G) = \mathbb{E}_{x,y}[\|y - G(x)\|_1] \quad (2)$$

Combining Eq.(1) and Eq.(2) yields the following minimax objective:

$$G^* = \arg \min_G \max_D \lambda_{adv} \mathcal{L}_{cGAN}(G, D) + \lambda_{L1} \mathcal{L}_{L1}(G) \quad (3)$$

Here, $\lambda_{adv} = 1$ and $\lambda_{L1} = 100$ are loss weighting terms selected based on favourable results from earlier research (Isola et al., 2017), (Dalmaz et al., 2022).

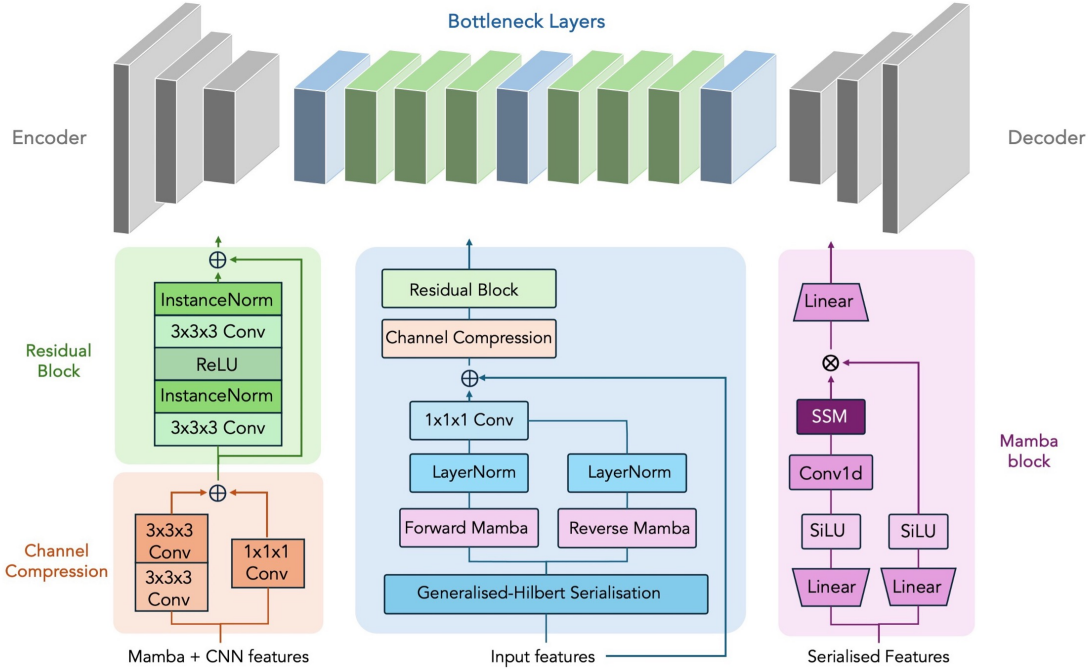


Figure 2: Generator Architecture. Bottleneck layers 1, 5 and 9 (light blue) include forward and reverse Mamba blocks, channel compression and residual blocks. Remaining bottleneck layers (light green) are comprised of a residual block only.

3.3. Experiments

3.3.1. DATA AND TRAINING

MRI data used in this paper stem from two separate studies on neurodevelopment over the first 3 years of life in LMICs. The Khula Study (Zieff et al., 2024) investigates the development of executive function in children based in South Africa and Malawi. Children with no known neurological abnormalities were scanned at ages of 3, 6, 12, 18, or 24 months.

Subjects attended two scanning sessions, with HF T₂w scans (1×1×1mm) acquired using a Siemens 3T scanner (Erlangen, DE) and ULF T₂w scans (1.5×1.5×5mm) acquired using a Hyperfine Swoop 64mT system (Guildford, CT). MINE (Maternal and environmental Impact assessment on Neurodevelopment in Early childhood years; [Surani et al. 2023](#)) assesses children based in Karachi, Pakistan, beginning at ages of 1, 3, or 6 months and continuing via yearly follow-ups. Subjects also attended two scanning sessions, with HF T₂w scans (0.5×0.5×0.5mm) acquired using a Toshiba 3T scanner (Otagawa, JP) and ULF T₂w scans (1.6×1.6×5mm) also acquired using a Hyperfine Swoop 64mT system (Guildford, CT).

Images were assessed for motion or banding artifacts; those with severe distortions were excluded, resulting in a total of 215 paired ULF and HF scans (116 Male, 99 Female; mean age 10.9 ± 6.7 months). Pre-processing involved rigid registration ([Avants et al., 2009](#)) of all HF scans to a custom age-specific HF template, and of each subject’s ULF scan to the corresponding pre-registered HF scan. We additionally resampled all ULF and HF scans to 1×1×1mm resolution to ensure consistency across scanners and sites. The data were split into training/validation/test sets of 137/35/43 scans (i.e. $\sim 64/16/20\%$), balancing for age and sex, and our model was trained for 1000 epochs on a Nvidia RTX 3090 24GB GPU. We used the Adam optimizer with $\beta_1 = 0.5$, $\beta_2 = 0.999$ and a learning rate of 0.0002. Patch-wise training was conducted, extracting random 128×128×128 patches from input and target images at each training step, and batch size was set to 1. During training, image augmentation was carried out on the fly, including random 3D rotation, BSpline deformation, random flip, and contrast and brightness adjustment.

3.3.2. COMPETING METHODS

To compare performance of our model to similar generator architectures, we trained three additional models from scratch using our data: SwinUNETR-V2 ([He et al., 2023](#)), ResViT ([Dalmaz et al., 2022](#)), and U-Mamba ([Ma et al., 2024](#)). These networks all combine local and global context; SwinUNETR-V2 merges the U-Net architecture with Swin-transformers, ResViT adds pre-trained vision transformers into bottleneck layers of a 9-block ResNet, and U-Mamba adds SSM blocks to each encoding layer of the U-Net. As ResViT was not designed to handle 3D data, we provide a 3D implementation here (details in Appendix C). For a fair comparison, all competing methods were implemented as adversarial models with a PatchGAN discriminator, trained via the loss function described in Eq.(3). The quality of model outputs relative to ground-truth HF images is evaluated via normalised root mean squared error (NRMSE), peak signal-to-noise ratio (PSNR), structural similarity index measure (SSIM), and learned perceptual image patch similarity (LPIPS).

We additionally benchmark against other existing ULF SR models; LF-SynthSR and SFNet. LoHiResGAN does not have publicly available weights for a model pre-trained on T₂w scans, and thus is excluded from benchmarking. As LF-SynthSR exclusively outputs T₁w MRI scans regardless of the contrast of the input, we compare outputs of GAMBAS and SFNet with those of LF-SynthSR via Dice overlap of segmented brain regions, using segmentations obtained via SynthSeg ([Billot et al., 2023](#)), a toolkit that is agnostic to contrast and resolution. Segmentation outputs for subjects at 3 months of age and younger (n=10) were highly inconsistent, therefore these were excluded from analyses. Unless otherwise specified, all significance testing was carried out via the Wilcoxon signed-rank test.

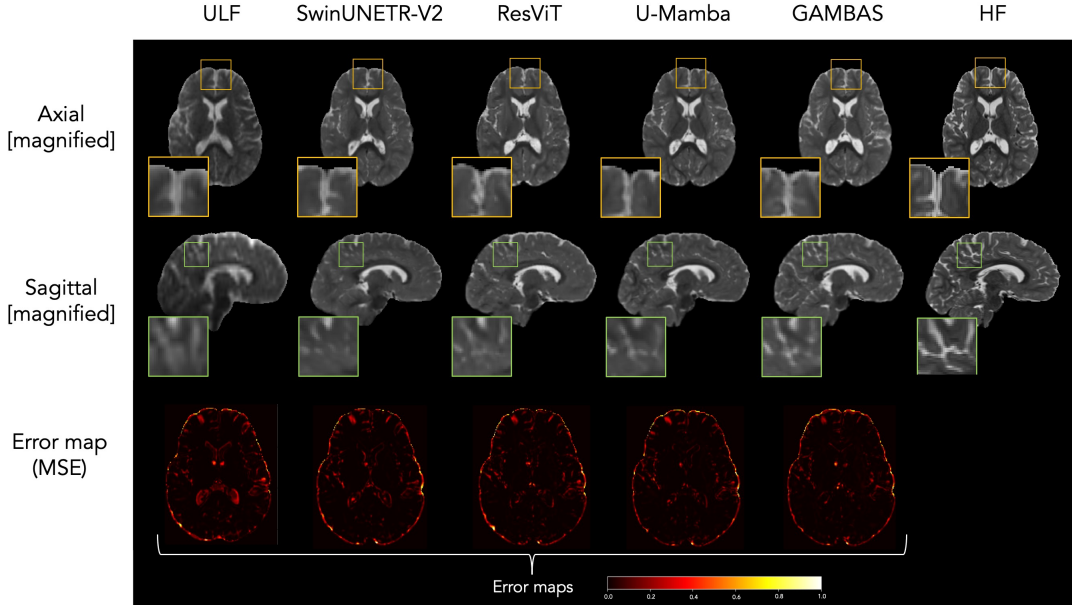


Figure 3: Model outputs and error maps from a single test subject. Left to right: raw ULF scan, SwinUNETR-V2, ResViT, U-Mamba, GAMBAS, reference HF scan.

4. Results

From our comparative analyses, we demonstrate that GAMBAS produces visually superior outputs compared to other models assessed (Figure 3). We highlight this with improved performance in all voxelwise metrics compared to SwinUNETR-V2, ResViT, and U-Mamba (Table 1), with GAMBAS improving ULF scores on average by 23.9%. Taking a more overarching view of the results, we additionally observe a pattern whereby Mamba-infused models (U-Mamba and GAMBAS) outperform transformer-infused models (SwinUNETR-V2 and ResViT), potentially signifying that Mamba is better suited for capturing global context in this image translation task. When assessing our performance against existing ULF SR models, segmentation-based analyses reveal that GAMBAS outperforms the only publicly available SR toolkits for use on 64mT ULF scans (LF-SynthSR and SFNet). Across all four tissue types (GMC, GMS, WM, CSF), GAMBAS demonstrates closest correspondence in Dice overlap to HF scans ($\mu=0.788$); higher than both SFNet ($\mu=0.691$) and LF-SynthSR ($\mu=0.693$); see Table 2 and Appendix E.

5. Discussion

Our novel GAMBAS network presents an effective and reliable method for translation of ULF to HF MRI, underscoring the potential for deep learning tools in widening accessibility to MRI in resource-limited settings. We demonstrate improved performance compared to other SOTA methods, highlighting the benefits conferred by our approach of fusing novel

Table 1: Image quality metrics for ULF scans and all SR methods trained using our dataset. Asterisk reflects a significant difference compared to all previous methods.

Model	NRMSE (\downarrow)	PSNR (\uparrow)	SSIM (\uparrow)	LPIPS (\downarrow)
none [ULF]	0.441 \pm 0.038	26.772 \pm 1.372	0.896 \pm 0.021	0.0402 \pm .0075
SwinUNETR-V2	0.315 \pm 0.044	29.750 \pm 1.827	0.911 \pm 0.017	0.0231 \pm .0047
ResViT	0.310 \pm 0.046	29.885 \pm 1.811	0.911 \pm 0.016	0.0235 \pm .0046
U-Mamba	0.294 \pm 0.043	30.336 \pm 1.868	0.914 \pm 0.016	0.0226 \pm .0050
GAMBAS	0.290\pm0.044	30.469\pm1.919	0.916\pm0.016*	0.0220\pm.0051*

Table 2: Dice coefficients for four tissue types: cortical grey matter (GMC), subcortical grey matter (GMS), white matter (WM) and cerebrospinal fluid (CSF), for input ULF scans, SynthSR and GAMBAS.

Model	GMC	GMS	WM	CSF
none [ULF]	0.682 \pm 0.055	0.680 \pm 0.216	0.698 \pm 0.097	0.423 \pm 0.069
LF-SynthSR	0.716 \pm 0.032	0.840 \pm 0.102	0.778 \pm 0.025	0.439 \pm 0.062
SFNet	0.731 \pm 0.036	0.794 \pm 0.083	0.759 \pm 0.042	0.478 \pm 0.061
GAMBAS	0.806\pm0.021*	0.899\pm0.014*	0.815\pm0.017*	0.631\pm0.051*

Generalised-Hilbert Mamba blocks with CNNs for image generation. Although U-Mamba also presents a network combining CNN and Mamba modules, they rely on a simple ‘Raster’ trajectory for 1D serialisation and do not include channel mixing blocks between CNN and Mamba outputs.

By training models with a paediatric dataset, we tackle a particularly challenging image translation task. Our data includes children scanned at various stages of brain development, from early stages of myelination with inverted GM:WM signal intensities relative to adult contrast (Dubois et al., 2021), through a period of strong overlap in tissue intensity (Bui et al., 2020), to later stages of myelination (1 year and above) when adult contrast is established. In spite of this, we demonstrate improved NRMSE, PSNR, SSIM, and LPIPS on a test set spanning subjects across all stages. One notable limitation of our study stems from our use of SynthSeg (Billot et al., 2023) for segmentation. It was chosen as it is the only widely available segmentation toolkit agnostic to contrast and resolution. However, as SynthSeg was trained on adult data, it performs poorly on scans deviating too much from the normal adult contrast, necessitating the exclusion of 3-month-old subjects from segmentation-based analyses.

In summary, GAMBAS shows great promise for SR of ULF MRI. Future work will explore its application to other datasets, including adult and/or clinical populations.

Acknowledgments

We would like to acknowledge funding from Artificial Intelligence Methods for Low Field MRI Enhancement, Bill and Melinda Gates Foundation (INV-032788) and Wellcome Leap 1kD programme (The First 1000 Days) [222076/Z/20/Z].

References

- Karim Armanious, Chenming Jiang, Marc Fischer, Thomas Küstner, Tobias Hepp, Konstantin Nikolaou, Sergios Gatidis, and Bin Yang. Medgan: Medical image translation using gans. *Computerized Medical Imaging and Graphics*, 79:101684, 2020. ISSN 0895-6111. doi: <https://doi.org/10.1016/j.compmedimag.2019.101684>. URL <https://www.sciencedirect.com/science/article/pii/S0895611119300990>.
- Thomas Campbell Arnold, Colbey W. Freeman, Brian Litt, and Joel M. Stein. Low-field mri: Clinical promise and challenges. *Journal of Magnetic Resonance Imaging*, 57(1): 25–44, 2023. doi: <https://doi.org/10.1002/jmri.28408>. URL <https://onlinelibrary.wiley.com/doi/abs/10.1002/jmri.28408>.
- Omer F. Atli, Bilal Kabas, Fuat Arslan, Mahmut Yurt, Onat Dalmaz, and Tolga Çukur. I2i-mamba: Multi-modal medical image synthesis via selective state space modeling. *arXiv:2405.14022*, 2024.
- Brian B Avants, Nick Tustison, and Hans Johnson. Advanced Normalization Tools (ANTS). *Insight j*, 2(365):1–35, 2009. URL https://psychiatry.ucsd.edu/research/programs-centers/snl/_files/ants2.pdf.
- Benjamin Billot, Douglas N. Greve, Oula Puonti, Axel Thielscher, Koen Van Leemput, Bruce Fischl, Adrian V. Dalca, and Juan Eugenio Iglesias. Synthseg: Segmentation of brain mri scans of any contrast and resolution without retraining. *Medical Image Analysis*, 86:102789, 2023. ISSN 1361-8415. doi: <https://doi.org/10.1016/j.media.2023.102789>. URL <https://www.sciencedirect.com/science/article/pii/S1361841523000506>.
- Toan Duc Bui, Li Wang, Weili Lin, Gang Li, and Dinggang Shen. 6-month infant brain mri segmentation guided by 24-month data using cycle-consistent adversarial networks. *2020 IEEE 17th International Symposium on Biomedical Imaging (ISBI)*, pages 359–362, 2020. URL <https://api.semanticscholar.org/CorpusID:218893283>.
- Adrienne E. Campbell-Washburn, Rajiv Ramasawmy, Matthew C. Restivo, Ipshita Bhattacharya, Burcu Basar, Daniel A. Herzka, Michael S. Hansen, Toby Rogers, W. Patricia Bandettini, Delaney R. McGuirt, Christine Mancini, David Grodzki, Rainer Schneider, Waqas Majeed, Himanshu Bhat, Hui Xue, Joel Moss, Ashkan A. Malayeri, Elizabeth C. Jones, Alan P. Koretsky, Peter Kellman, Marcus Y. Chen, Robert J. Lederman, and Robert S. Balaban. Opportunities in interventional and diagnostic imaging by using high-performance low-field-strength mri. *Radiology*, 293(2):384–393, 2019. doi: [10.1148/radiol.2019190452](https://doi.org/10.1148/radiol.2019190452). URL <https://doi.org/10.1148/radiol.2019190452>. PMID: 31573398.

- M. Jorge Cardoso, Wenqi Li, Richard Brown, Nic Ma, Eric Kerfoot, Yiheng Wang, Benjamin Murrey, Andriy Myronenko, Can Zhao, Dong Yang, Vishwesh Nath, Yufan He, Ziyue Xu, Ali Hatamizadeh, Andriy Myronenko, Wentao Zhu, Yun Liu, Mingxin Zheng, Yucheng Tang, Isaac Yang, Michael Zephyr, Behrooz Hashemian, Sachidanand Alle, Mohammad Zalbagi Darestani, Charlie Budd, Marc Modat, Tom Vercauteren, Guotai Wang, Yiwen Li, Yipeng Hu, Yunguan Fu, Benjamin Gorman, Hans Johnson, Brad Genereaux, Barbaros S. Erdal, Vikash Gupta, Andres Diaz-Pinto, Andre Dourson, Lena Maier-Hein, Paul F. Jaeger, Michael Baumgartner, Jayashree Kalpathy-Cramer, Mona Flores, Justin Kirby, Lee A. D. Cooper, Holger R. Roth, Daguang Xu, David Bericat, Ralf Floca, S. Kevin Zhou, Haris Shuaib, Keyvan Farahani, Klaus H. Maier-Hein, Stephen Aylward, Prerna Dogra, Sebastien Ourselin, and Andrew Feng. Monai: An open-source framework for deep learning in healthcare, 2022. URL <https://arxiv.org/abs/2211.02701>.
- Wanli Chen, Xinge Zhu, Guojin Chen, and Bei Yu. Efficient point cloud analysis using hilbert curve. In *2022 European Conference on Computer Vision (ECCV)*, page 5428–5437, 2022. doi: https://doi.org/10.1007/978-3-031-20086-1_42.
- Onat Dalmaz, Mahmut Yurt, and Tolga Çukur. Resvit: Residual vision transformers for multimodal medical image synthesis. *IEEE Transactions on Medical Imaging*, 41(10): 2598–2614, 2022. doi: 10.1109/TMI.2022.3167808.
- Alexey Dosovitskiy, Lucas Beyer, Alexander Kolesnikov, Dirk Weissenborn, Xiaohua Zhai, Thomas Unterthiner, Mostafa Dehghani, Matthias Minderer, Georg Heigold, Sylvain Gelly, Jakob Uszkoreit, and Neil Houlsby. An image is worth 16x16 words: Transformers for image recognition at scale. In *International Conference on Learning Representations*, 2021. URL <https://openreview.net/forum?id=YicbFdNTTy>.
- Jessica Dubois, Marianne Alison, Serena J. Counsell, Lucie Hertz-Pannier, Petra S. Hüppi, and Manon J.N.L. Benders. Mri of the neonatal brain: A review of methodological challenges and neuroscientific advances. *Journal of Magnetic Resonance Imaging*, 53(5):1318–1343, 2021. doi: <https://doi.org/10.1002/jmri.27192>. URL <https://onlinelibrary.wiley.com/doi/abs/10.1002/jmri.27192>.
- Albert Gu and Tri Dao. Mamba: Linear-time sequence modeling with selective state spaces. *arXiv preprint arXiv:2312.00752*, 2023.
- Albert Gu, Karan Goel, and Christopher Ré. Efficiently modeling long sequences with structured state spaces. In *The International Conference on Learning Representations (ICLR)*, 2022.
- Kaiming He, Xiangyu Zhang, Shaoqing Ren, and Jian Sun. Deep residual learning for image recognition. In *2016 IEEE Conference on Computer Vision and Pattern Recognition (CVPR)*, pages 770–778, 2016. doi: 10.1109/CVPR.2016.90. URL <https://ieeexplore.ieee.org/document/7780459>.
- Yufan He, Vishwesh Nath, Dong Yang, Yucheng Tang, Andriy Myronenko, and Daguang Xu. Swinunetr-v2: Stronger swin transformers with stagewise convolutions for 3d medical image segmentation. In *MICCAI (4)*, pages 416–426, 2023. URL https://doi.org/10.1007/978-3-031-43901-8_40.

- Moein Heidari, Sina Ghorbani Kolahi, Sanaz Karimijafarbigloo, Bobby Azad, Afshin Bozorgpour, Soheila Hatami, Reza Azad, Ali Diba, Ulas Bagci, Dorit Merhof, and Ilker Hacıhaliloglu. Computation-efficient era: A comprehensive survey of state space models in medical image analysis, 2024. URL <https://arxiv.org/abs/2406.03430>.
- David R. Hilbert. Ueber die stetige abbildung einer line auf ein flächenstück. *Mathematische Annalen*, 38:459–460, 1891. URL <https://api.semanticscholar.org/CorpusID:123643081>.
- Juan Eugenio Iglesias, Benjamin Billot, Yaël Balbastre, Azadeh Tabari, John Conklin, R. Gilberto González, Daniel C. Alexander, Polina Golland, Brian L. Edlow, and Bruce Fischl. Joint super-resolution and synthesis of 1mm isotropic mp-rage volumes from clinical mri exams with scans of different orientation, resolution and contrast. *NeuroImage*, 237:118206, 2021. ISSN 1053-8119. doi: <https://doi.org/10.1016/j.neuroimage.2021.118206>. URL <https://www.sciencedirect.com/science/article/pii/S1053811921004833>.
- Juan Eugenio Iglesias, Riana Schleicher, Sonia Laguna, Benjamin Billot, Pamela Schaefer, Brenna McKaig, Joshua N. Goldstein, Kevin N. Sheth, Matthew S. Rosen, and W. Taylor Kimberly. Quantitative brain morphometry of portable low-field-strength mri using super-resolution machine learning. *Radiology*, 306(3):e220522, 2023. doi: [10.1148/radiol.220522](https://doi.org/10.1148/radiol.220522). URL <https://doi.org/10.1148/radiol.220522>.
- Fabian Isensee, Jens Petersen, André Klein, David Zimmerer, Paul F. Jaeger, Simon Kohl, Jakob Wasserthal, Gregor Köhler, Tobias Norajitra, Sebastian J. Wirkert, and Klaus H. Maier-Hein. nnu-net: Self-adapting framework for u-net-based medical image segmentation. *CoRR*, abs/1809.10486, 2018. URL <http://arxiv.org/abs/1809.10486>.
- Kh Tohidul Islam, Shenjun Zhong, Parisa Zakavi, Zhifeng Chen, Helen Kavnoudias, Shawna Farquharson, Gail Durbridge, Markus Barth, Katie L. McMahon, Paul M. Parizel, Andrew Dwyer, Gary F. Egan, Meng Law, and Zhaolin Chen. Improving portable low-field mri image quality through image-to-image translation using paired low- and high-field images. *Scientific Reports*, 13(1), 2023. ISSN 2045-2322. doi: [10.1038/s41598-023-48438-1](https://doi.org/10.1038/s41598-023-48438-1).
- Phillip Isola, Jun-Yan Zhu, Tinghui Zhou, and Alexei A. Efros. Image-to-image translation with conditional adversarial networks. In *2017 IEEE Conference on Computer Vision and Pattern Recognition (CVPR)*, pages 5967–5976, 2017. doi: [10.1109/CVPR.2017.632](https://doi.org/10.1109/CVPR.2017.632).
- Mohammad Jalloul, Monica Miranda-Schaeubinger, Abass M. Noor, Joel M. Stein, Raisa Amiruddin, Hermon Miliard Derbew, Victoria L. Mango, Adeyanju Akinola, Kelly Hart, Joseph Weygand, Erica Pollack, Sharon Mohammed, John R. Scheel, Jessica Shell, Farouk Dako, Pradnya Mhatre, Lauren Kulinski, Hansel J. Otero, and Daniel J. Mollura. Mri scarcity in low- and middle-income countries. *NMR in Biomedicine*, 36(12):e5022, 2023. doi: <https://doi.org/10.1002/nbm.5022>. URL <https://analyticalsciencejournals.onlinelibrary.wiley.com/doi/abs/10.1002/nbm.5022>.
- Jun Ma, Feifei Li, and Bo Wang. U-mamba: Enhancing long-range dependency for biomedical image segmentation. *arXiv preprint arXiv:2401.04722*, 2024.

- B. Moon, H.V. Jagadish, C. Faloutsos, and J.H. Saltz. Analysis of the clustering properties of the hilbert space-filling curve. *IEEE Transactions on Knowledge and Data Engineering*, 13(1):124–141, 2001. doi: 10.1109/69.908985.
- Jack A. Orenstein. Spatial query processing in an object-oriented database system. In *Proceedings of the 1986 ACM SIGMOD International Conference on Management of Data*, SIGMOD ’86, page 326–336, New York, NY, USA, 1986. Association for Computing Machinery. ISBN 0897911911. doi: 10.1145/16894.16886. URL <https://doi.org/10.1145/16894.16886>.
- Francesco Padormo, Paul Cawley, Louise Dillon, Emer Hughes, Jennifer Almalbis, Joanna Robinson, Alessandra Maggioni, Miguel De La Fuente Botella, Dan Cromb, Anthony Price, Lori Arlinghaus, John Pitts, Tianrui Luo, Dingtian Zhang, Sean C. L. Deoni, Steve Williams, Shaihan Malik, Jonathan O’Muirheartaigh, Serena J. Counsell, Mary Rutherford, Tomoki Arichi, A. David Edwards, and Joseph V. Hajnal. In vivo t mapping of neonatal brain tissue at 64 mt. *Magnetic Resonance in Medicine*, 89(3):1016–1025, 2023. doi: <https://doi.org/10.1002/mrm.29509>. URL <https://onlinelibrary.wiley.com/doi/abs/10.1002/mrm.29509>.
- Zoya Surani, Sadia Parkar, Gul Afshan, Kinza Naseem Elahi, Zahra Hoodbhoy, Kiran Hilal, and Sidra Kaleem Jafri. Maternal and environmental impact assessment on neurodevelopment in early childhood years (mine): a prospective cohort study protocol from a low, middle-income country. *BMJ Open*, 13(7), 2023. ISSN 2044-6055. doi: 10.1136/bmjopen-2022-070283. URL <https://bmjopen.bmj.com/content/13/7/e070283>.
- Austin Tapp, Can Zhao, Holger R. Roth, Jeffrey Tanedo, Syed Muhammad Anwar, Niall J. Bourke, Joseph V. Hajnal, Victoria Nankabirwa, Sean Deoni, Natasha Lepore, and Marius George Linguraru. Super-Field MRI Synthesis for Infant Brains Enhanced by Dual Channel Latent Diffusion . In *proceedings of Medical Image Computing and Computer Assisted Intervention – MICCAI 2024*, volume LNCS 15003. Springer Nature Switzerland, October 2024.
- Ilya Tolstikhin, Neil Houlsby, Alexander Kolesnikov, Lucas Beyer, Xiaohua Zhai, Thomas Unterthiner, Jessica Yung, Andreas Peter Steiner, Daniel Keysers, Jakob Uszkoreit, Mario Lucic, and Alexey Dosovitskiy. MLP-mixer: An all-MLP architecture for vision. In A. Beygelzimer, Y. Dauphin, P. Liang, and J. Wortman Vaughan, editors, *Advances in Neural Information Processing Systems*, 2021. URL <https://openreview.net/forum?id=EI2K0XKdnP>.
- Lu Wang, Hairui Wang, Yingna Huang, Baihui Yan, Zhihui Chang, Zhaoyu Liu, Mingfang Zhao, Lei Cui, Jiangdian Song, and Fan Li. Trends in the application of deep learning networks in medical image analysis: Evolution between 2012 and 2020. *European Journal of Radiology*, 146:110069, 2022. ISSN 0720-048X. doi: <https://doi.org/10.1016/j.ejrad.2021.110069>. URL <https://www.sciencedirect.com/science/article/pii/S0720048X21005507>.

- Zihao Wang and Lei Wu. Theoretical analysis of the inductive biases in deep convolutional networks. In *Thirty-seventh Conference on Neural Information Processing Systems*, 2023. URL <https://openreview.net/forum?id=NOKwVdaaaJ>.
- M. S. Warren and J. K. Salmon. A parallel hashed oct-tree n-body algorithm. In *Proceedings of the 1993 ACM/IEEE Conference on Supercomputing*, Supercomputing '93, page 12–21, New York, NY, USA, 1993. Association for Computing Machinery. ISBN 0818643404. doi: 10.1145/169627.169640. URL <https://doi.org/10.1145/169627.169640>.
- Guowen Zhang, Lue Fan, Chenhang He, Zhen Lei, Zhaoxiang Zhang, and Lei Zhang. Voxel mamba: Group-free state space models for point cloud based 3d object detection. *arXiv preprint arXiv:2406.10700*, 2024.
- Weilian Zhou, Sei ichiro Kamata, Haipeng Wang, Man Sing Wong, and Huiying (Cynthia) Hou. Mamba-in-mamba: Centralized mamba-cross-scan in tokenized mamba model for hyperspectral image classification. *Neurocomputing*, 613:128751, 2025. ISSN 0925-2312. doi: <https://doi.org/10.1016/j.neucom.2024.128751>. URL <https://www.sciencedirect.com/science/article/pii/S0925231224015224>.
- Jun-Yan Zhu, Taesung Park, Phillip Isola, and Alexei A. Efros. Unpaired image-to-image translation using cycle-consistent adversarial networks. In *2017 IEEE International Conference on Computer Vision (ICCV)*, pages 2242–2251, 2017. doi: 10.1109/ICCV.2017.244.
- MR Zieff, M Miles, E Mbale, E Eastman, L Ginnell, SCR Williams, DK Jones, DC Alexander, PA Wijeratne, LJ Gabard-Durnam, V Klepac-Ceraj, KS Bonham, N Pini, A Sania, M Lucchini, S Deoni, WP Fifer, M Gladstone, D Amso, and KA Donald. Characterizing developing executive functions in the first 1000 days in south africa and malawi: The khula study. *Wellcome Open Research*, 9(157), 2024. doi: 10.12688/wellcomeopenres.19638.1.
- Jakub Červený. Gilbert. <https://github.com/jakubcerveny/gilbert>, 2019. Accessed: 2024-12-01.

Appendix A. S4 and Mamba

The state space model (SSM) is a continuous-time latent state model, which maps a 1D input $x(t) \in \mathbb{R}^L$ to an output $y(t) \in \mathbb{R}^L$ through hidden state $h(t) \in \mathbb{R}^N$ via the following linear ODE:

$$\begin{aligned} h'(t) &= \mathbf{A}h(t) + \mathbf{B}x(t), \\ y(t) &= \mathbf{C}h(t) + \mathbf{D}x(t) \end{aligned} \tag{4}$$

Here, $\mathbf{A} \in \mathbb{R}^{N \times N}$, $\mathbf{B} \in \mathbb{R}^{N \times 1}$, and $\mathbf{C} \in \mathbb{R}^{1 \times N}$ are learnable parameters and $\mathbf{D} \in \mathbb{R}^1$ represents a residual connection. The continuous-time SSM has prohibitive computation and memory requirements for deep learning applications, however, it can be discretized using a timescale parameter Δ . For this, the zero-order hold (ZOH) technique is employed, whereby continuous parameters \mathbf{A} , \mathbf{B} are discretized as $\bar{\mathbf{A}} = \exp(\Delta\mathbf{A})$, $\bar{\mathbf{B}} = (\Delta\mathbf{A})^{-1}(\exp(\Delta\mathbf{A}) - \mathbf{I}) \cdot \Delta\mathbf{B}$. By substituting these into Eq.(4), we obtain the structured state-space sequence model, or S4 (Gu et al., 2022), represented in the following recurrent form:

$$\begin{aligned} h_t &= \bar{\mathbf{A}}h_{t-1} + \bar{\mathbf{B}}x_t, \\ y_t &= \mathbf{C}h_t + \mathbf{D}x_t \end{aligned} \tag{5}$$

Given an input $x \in \mathbb{R}^{1 \times L}$, where L is the sequence length, the model can also be computed by convolving a structured convolution kernel $\bar{\mathbf{K}} = (\mathbf{C}\bar{\mathbf{B}}, \mathbf{C}\bar{\mathbf{A}}\bar{\mathbf{B}}, \dots, \mathbf{C}\bar{\mathbf{A}}^L\bar{\mathbf{B}})$ across x . Although efficient for training, S4 is unable to select data in an input-dependent manner.

Mamba overcomes this hurdle and distinguishes itself from earlier SSMs by setting the model parameters to be input-dependent, endowing the model with a selection mechanism that can filter out irrelevant information and remember relevant information indefinitely (Gu and Dao, 2023). This no longer allows for the convolutional formulation to be applied (as input-dependent parameters prevent the use of a single structured kernel), however efficient training is ensured via a hardware-aware algorithm that computes model outputs using a parallel scan operation.

Appendix B. Hilbert curve and implementation

The Hilbert curve can be expressed concisely using a Lindenmayer system, or L-system. L-systems consist of three components: 1) an “alphabet” of symbols that form a string, 2) an initial “axiom” string, and 3) a set of “production rules” that describe how symbols are replaced to form a larger string. Crucially, the “alphabet” can be sub-divided into “variables” (symbols that can be replaced) and “constants” (symbols that cannot be replaced). Once a string evolves through a number of successive iterations from the axiom via the production rules, the output is used as a set of instructions for generating a geometric structure. The L-system describing the Hilbert curve can be summarised as:

$$\begin{aligned}
 \text{Variables} &= A, B \\
 \text{Constants} &= F, +, - \\
 \text{Axiom} &= A \\
 \text{Production rules} &= A \rightarrow +BF - AFA - FB+, \\
 &B \rightarrow -AF + BFB + FA-
 \end{aligned} \tag{6}$$

where F is forward, $-$ and $+$ indicate a 90° turn clockwise and counterclockwise, respectively, and A and B are ignored during drawing. The first three iterations of this L-system are depicted in Figure 4.

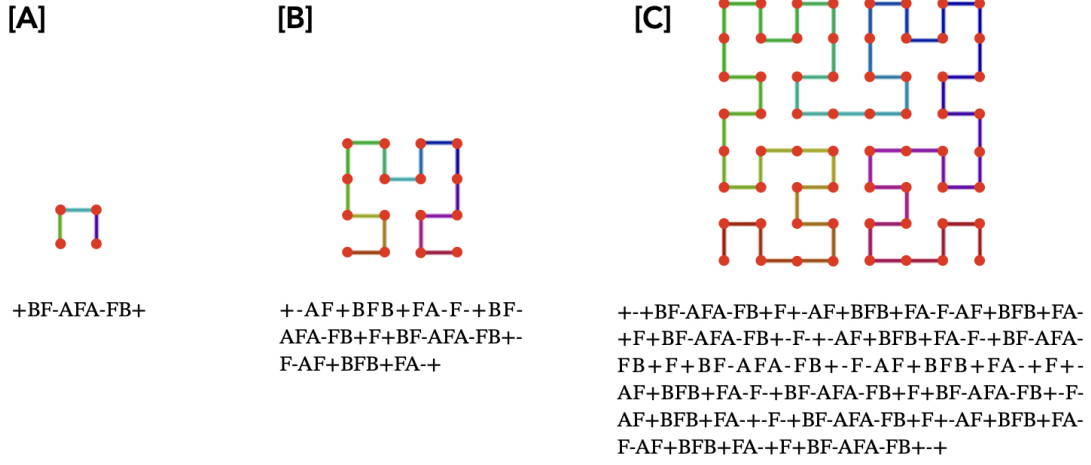


Figure 4: [A] Iteration 1, [B] iteration 2, and [C] iteration 3 of the Hilbert curve, following starting axiom A . The output string is shown on the bottom, and the corresponding geometric structure on top.

The original formulation of the Hilbert curve only produces structures composed of 4^n vertices to fill regions in 2D space (see Figure 4). By using a generalised formulation of the Hilbert curve (Červený, 2019), we instead are able to handle 3D image features of any even dimensions. This implementation uses a recursive mechanism to split a cuboid into multiple regions, with the function calling on itself until a trivial path can be computed. Calling this function in each training step would compromise efficiency, however we circumvent this by only using the function once upon model initialization, at which point a tensor is stored with indices that delineate the serialisation of 3D inputs with pre-specified dimensions. We operate with patches of size $128 \times 128 \times 128$, which are then downsampled through our encoder blocks to be of size $32 \times 32 \times 32$. As such, a Generalised Hilbert-curve for a cube with height, width and depth of 32 is computed and stored upon model initialisation, and is used in each training step to serialise 3D image features before being fed into forward and reverse Mamba blocks (Figure 2).

Appendix C. Implementation of competing methods

C.1. SwinUNETR-V2

SwinUNETR-V2 was implemented using the MONAI framework (Cardoso et al., 2022), with all parameters (i.e. network feature size, number of layers in each stage and number of attention heads) set to default settings, in line with the original paper (He et al., 2023).

C.2. U-Mamba

As U-Mamba is implemented in the self-adapting nnU-Net (Isensee et al., 2018) framework, which is tailored for segmentation data, we examined the network configurations for various datasets listed in the original paper (Ma et al., 2024) and selected the one most closely aligned with our own data (3D Abdomen MRI). Consequently, we used the “U-Mamba_Enc” variant (employing Mamba blocks in all encoder layers), with 6 encoder/decoder stages and pooling per axis set at (3, 5, 5).

C.3. ResViT

ResViT used an identical 9-block ResNet backbone as GAMBAS, however transformer modules were inserted into bottleneck layers 1 and 4, in accordance with the original paper. These modules used weights from transformer component of the ImageNet-pretrained model R50+ViT-B/16 (https://github.com/google-research/vision_transformer). As the pre-trained transformer expects 2D inputs of size 16×16 , we downsampled image features in transformer blocks to match the desired height and width, and performed patch embedding across the depth dimension.

Appendix D. Ablation studies

D.1. Insertion of Mamba blocks

Table 3: Ablations on the number of mamba blocks inserted into the bottleneck layers of GAMBAS. (1,5,9) denotes mamba blocks in the first, fifth, and ninth layers.

Model	NRMSE (\downarrow)	PSNR (\uparrow)	SSIM (\uparrow)	μ Dice (\uparrow)
none	0.314 \pm 0.053	30.185 \pm 1.403	0.7795 \pm .0141	0.7795 \pm .0339
(5)	0.312 \pm 0.054	30.254 \pm 1.489	0.9149 \pm .0143	0.7766 \pm .0352
(1,5,9)	0.311\pm0.055	30.285\pm1.482	0.9162\pm.0140	0.7802\pm.0363
(1,3,5,7,9)	0.315 \pm 0.057	30.116 \pm 1.518	0.9153 \pm .0141	0.7760 \pm .0336
(1,2,3,...9)	0.312 \pm 0.052	30.185 \pm 1.432	0.9160 \pm .0139	0.7782 \pm .0349

D.2. Scanning trajectory

Table 4: Ablation on scanning trajectory used by bidirectional mamba blocks in first, middle, and final bottleneck layers.

Serialisation	NRMSE (\downarrow)	PSNR (\uparrow)	SSIM (\uparrow)	μ Dice (\uparrow)
Raster	0.315 \pm 0.061	30.195 \pm 1.598	0.9157 \pm .0141	0.7782 \pm .0350
Generalised-Hilbert	0.311\pm0.055	30.285\pm1.482	0.9162\pm.0140	0.7802\pm.0363

D.3. Unidirectional vs bidirectional mamba

Table 5: Ablation on the use of bidirectional mamba for mamba blocks in first, middle, and final bottleneck layers.

Model	NRMSE (\downarrow)	PSNR (\uparrow)	SSIM (\uparrow)	μ Dice (\uparrow)
Unidirectional	0.311\pm0.052	30.265 \pm 1.458	0.9160 \pm .0140	0.7792 \pm .0353
Bidirectional	0.311\pm0.055	30.285\pm1.827	0.9162\pm.0140	0.7802\pm.0363

Appendix E. Segmentations

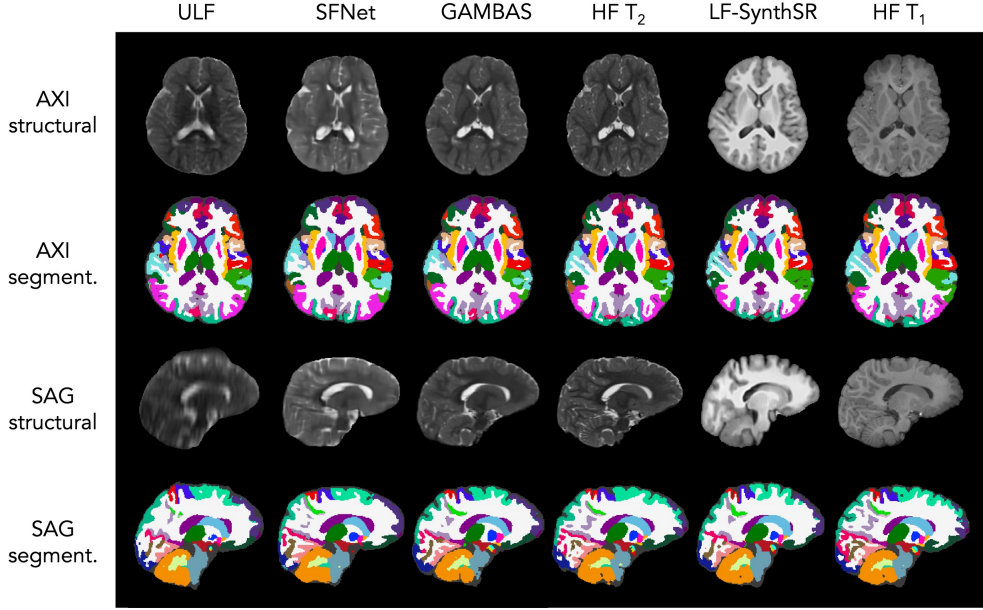


Figure 5: Model outputs and segmentations from a single test subject. Left to right: raw ULF scan, SFNet, GAMBAS, reference T₂w HF scan, SynthSR, reference T₁w HF scan.

Appendix F. Bias across sites

Table 6: Model performance across the two imaging sites: South Africa (Khula study) and Pakistan (MINE study). Significance testing, carried out via the Mann-Whitney U-Test, showed no significant differences.

Imaging site	NRMSE (\downarrow)	PSNR (\uparrow)	SSIM (\uparrow)	μ Dice(\uparrow)
Khula	0.298 ± 0.051	30.146 ± 2.462	0.913 ± 0.016	0.789 ± 0.024
MINE	0.282 ± 0.031	30.884 ± 1.272	0.917 ± 0.015	0.786 ± 0.018
p-value	0.312	0.473	0.551	0.503

Appendix G. Generalisation to adult data

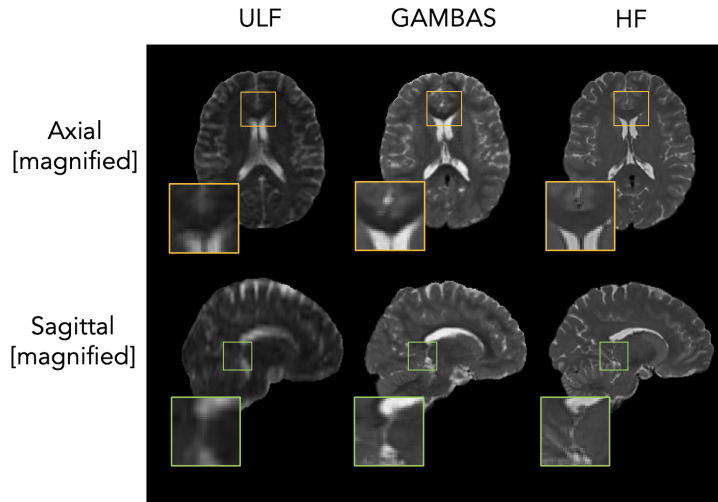


Figure 6: Model outputs from a single adult subject. Left to right: raw ULF scan, GAMBAS, reference HF scan.

Table 7: Image quality metrics for ULF scans and GAMBAS, as determined from a dataset of 20 healthy adult subjects scanned on ULF and HF scanners.

Model	NRMSE (\downarrow)	PSNR (\uparrow)	SSIM (\uparrow)	LPIPS (\downarrow)
none [ULF]	0.521 ± 0.032	24.194 ± 0.806	$0.839 \pm .0018$	$0.0473 \pm .0038$
GAMBAS	0.476 ± 0.074	25.054 ± 1.281	$0.850 \pm .0018$	$0.0349 \pm .0035$

Appendix H. Generalisation to pathological data

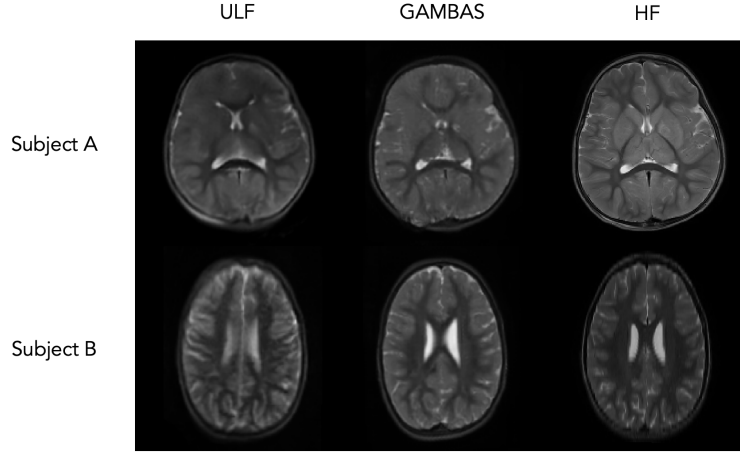


Figure 7: Model outputs from two separate paediatric subjects with known pathologies. Subject A: Hypoxia after strangulation; Subject B: Parechovirus encephalitis. We thank Professor Hemmen Sabir, Head of Experimental Neonatology at the University Hospital Bonn, for providing the following assessment: *“In Subject A, the HF image contains very obvious global brain swelling and injury to cortex and Basal ganglia. It is also seen on the ULF image, but much more obviously on the SR image. In subject B I see cortical highlighting in the pre-central cortex [in the HF image]. I can also see this in the ULF image (a bit blurry), but [...] even a bit better in the SR image.”*

Appendix I. Failed outputs

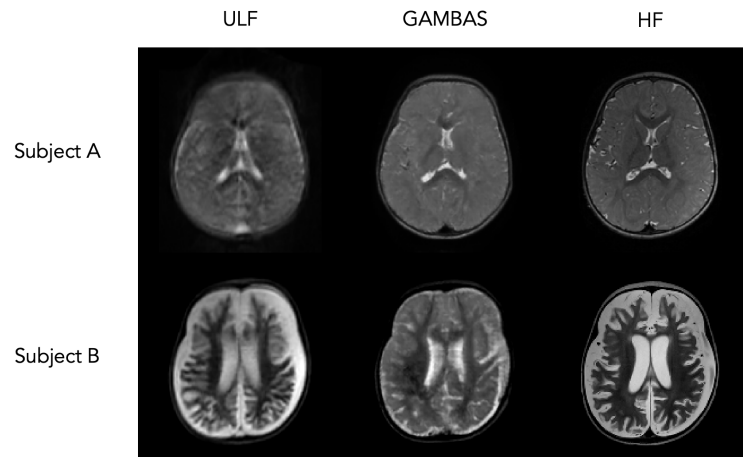


Figure 8: Poor quality model outputs from two separate cases. Subject A has a severe motion-corrupted ULF scan (excluded from the training set), whereas subject B is diagnosed with subdural hygroma, resulting in an ULF scan with significantly different contrast compared to healthy subjects.